International Journal of Nanomedicine

Dovepress
open access to scientific and medical research

Open Access Full Text Article

ORIGINAL RESEARCH

Theranostic Nanoparticles with Aggregation-Induced Emission and MRI Contrast Enhancement Characteristics as a Dual-Modal Imaging Platform for Image-Guided Tumor Photodynamic Therapy

This article was published in the following Dove Press journal:
International Journal of Nanomedicine

Huikang Yang,[1]* Yufang He,[1]* Yan Wang,[2]* Ruimeng Yang,[1] Nianhua Wang,[1] Li-Ming Zhang,[3]* Meng Gao,[4] Xinqing Jiang[1]

[1]Department of Radiology, Guangzhou First People's Hospital, School of Medicine, South China University of Technology, Guangzhou, Guangdong Province 510640, People's Republic of China; [2]Department of Urology, Guangzhou First People's Hospital, School of Medicine, South China University of Technology, Guangzhou, Guangdong Province 510640, People's Republic of China; [3]School of Materials Science and Engineering, Sun Yat-sen University, Guangzhou, Guangdong Province 510275, People's Republic of China; [4]National Engineering Research Center for Tissue Restoration and Reconstruction, South China University of Technology, Guangzhou, Guangdong Province 510006, People's Republic of China

*These authors contributed equally to this work

Correspondence: Xinqing Jiang
Department of Radiology, Guangzhou First People's Hospital, School of Medicine, South China University of Technology, Yuexiu District, Guangzhou, Guangdong Province 510640, People's Republic of China
Tel/Fax +86 13802961338
Email eyjiangxq@scut.edu.cn

Meng Gao
National Engineering Research Center for Tissue Restoration and Reconstruction, South China University of Technology, Tianhe District, Guangzhou, Guangdong Province 510006, People's Republic of China
Tel/Fax +86 15521393090
Email msmgao@scut.edu.cn

Introduction: Advanced tumor-targeted theranostic nanoparticles play a key role in tumor diagnosis and treatment research. In this study, we developed a multifunctional theranostic platform based on an amphiphilic hyaluronan/poly-(*N*-ε-carbobenzyloxy-L-lysine) derivative (HA-*g*-PZLL), superparamagnetic iron oxide (SPIO) and aggregation-induced emission (AIE) nanoparticles for tumor-targeted magnetic resonance (MR) and fluorescence (FL) dual-modal image-guided photodynamic therapy (PDT).

Materials and Methods: The amphiphilic hyaluronan acid (HA) derivative HA-*g*-PZLL was synthesized by grafting hydrophobic poly-(*N*-ε-carbobenzyloxy-L-lysine) (PZLL) blocks onto hyaluronic acid by a click conjugation reaction. The obtained HA-*g*-PZLLs self-assembled into nanoparticles in the presence of AIE molecules and SPIO nanoparticles to produce tumor-targeted theranostic nanoparticles (SPIO/AIE@HA-*g*-PZLLs) with MR/FL dual-modal imaging ability. Cellular uptake of the theranostic nanoparticles was traced by confocal laser scanning microscopy (CLSM), flow cytometry and Prussian blue staining. The intracellular reactive oxygen species (ROS) generation characteristics of the theranostic nanoparticles were evaluated with CLSM and flow cytometry. The effect of PDT was evaluated by cytotoxicity assay. The dual-mode imaging ability of the nanoparticles was evaluated by a real-time near-infrared fluorescence imaging system and magnetic resonance imaging scanning.

Results: The resulting theranostic nanoparticles not only emit red fluorescence for high-quality intracellular tracing but also effectively produce singlet oxygen for photodynamic tumor therapy. In vitro cytotoxicity experiments showed that these theranostic nanoparticles can be efficiently taken up and are mainly present in the cytoplasm of HepG2 cells. After internalization, these theranostic nanoparticles showed serious cytotoxicity to the growth of HepG2 cells after white light irradiation.

Discussion: This work provides a simple method for the preparation of theranostic nanoparticles with AIE characteristics and MR contrast enhancement, and serves as a dual-modal imaging platform for image-guided tumor PDT.

Keywords: aggregation-induced emission, MR imaging, dual-modal imaging, photodynamic therapy

Introduction

Recently, theranostic nanoparticles with tumor-targeting ability, strong magnetization and fluorescent properties have attracted much attention in the field of tumor diagnosis and treatment. This system could provide real-time therapy information in

a noninvasive manner. Moreover, medical staff can adjust the treatment plan according to the actual situation of patients to reach the goal of individualized treatment.[1–7] However, developing such an ideal theranostic platform still faces many challenges. For example, how to enhance contrast agents or drug water solubility, prolong the in vivo circulation time, maximize the accumulation in tumor tissue and reduce the adverse effects.[8]

It is well known that polymeric nanoparticles can enhance guest molecule water solubility, prolong blood circulation time and improve specific accumulation in tumor tissue via passive targeting (enhanced permeability and retention (EPR) effect) or active targeting (receptor–ligand interaction).[9,10] Therefore, polymeric nanoparticles show great potential as theranostic tools to deliver drugs or contrast agents to tumor tissue for treatment or imaging.[11,12] However, passive targeting with low selectivity would reduce the bioavailability and cause side effects. To overcome the above drawbacks of passive targeting, a series of targeting molecules, such as folic acid, antibodies, peptides and carbohydrates, have been introduced into polymeric nanoparticles.[13,14] As a natural polysaccharide, hyaluronan (HA) not only has high water solubility and biocompatibility but also targets CD44.[15,16] Therefore, HA and its derivatives play an important role in targeted drug or contrast agent delivery. For example, hyaluronan-block-poly(γ-benzyl glutamate) copolymers were prepared by Lecommandoux and coworkers and acted as multifunctional nanocarriers for drug delivery.[17] Daniela and coworkers found that superparamagnetic iron oxide (SPIO)-loaded hyaluronan polymeric micelles show selective anticancer effects towards a number of human cancer cell lines, and the in vivo intramuscular tumor accumulation of SPIO could be detected by MR imaging.[18] Theranostic nanoparticles based on hyaluronan-modified superparamagnetic iron oxide nanoparticles (HA-SPIO) were prepared by Yang et al, and HA-SPIO not only showed tumor-targeting capacity but also exhibited excellent T_2-weighted MR contrast enhancement and photothermal therapy abilities.[19] Disulfide bond-linked hyaluronan-SS-poly(ε-caprolactone) block copolymers were prepared by Yang et al after loading DOX and SPIO and acted as theranostic nanocarriers to load doxorubicin and SPIO for tumor diagnosis and treatment.[20]

As a noninvasive modern biomedical imaging technology, MR imaging possesses several advantages such as high spatial and temporal resolution, excellent soft tissue penetration depth and no potential radiation damage. However, MR imaging still suffers from low sensitivity.[21] To obtain high-resolution and sensitive diagnostic information, the development trend of MR imaging-based molecular imaging technology has developed from a single-mode imaging system to a dual-mode or multimode imaging system.[22–24] For instance, many imaging modalities such as computed tomography (CT), positron-emission tomography (PET), ultrasonic imaging and FL imaging have been combined with MR imaging to develop dual-modal or multimodal imaging systems.[25] Among them, the combination of MR/FL dual-modal imaging has captured great interest because these imaging techniques can offer the advantages of improving the relatively poor sensitivity of MR imaging and overcoming the detection depth and resolution limits of FL imaging.

In this context, theranostic nanoplatforms with MR/FL dual-modal imaging have been developed by integrating MR and FL imaging contrast agents into nanoparticles. In the past, luminous quantum dots (QDs) and commercial organic dyes have been used as FL imaging contrast agents. Although quantum dots have good photostability, they contain heavy metals and have potential biological toxicity.[26] Commercially available organic dyes, such as fluorescein isothiocyanate (FITC), porphyrin and Nile Red, have good biocompatibility and high emission efficiency. However, these organic dyes suffer from low fluorescence quantum yield or even fluorescence quenching at high concentrations or in the solid-state due to the aggregation-caused quenching (ACQ) effect.[27,28] Recently, a new kind of organic dye with AIE characteristics has received much attention owing to its high photochemical stability and quantum yield at high concentrations or in the aggregated state.[29] In recent years, a large variety of AIE-based bioprobes with MR imaging functions have been developed for biomedical imaging, diagnosis, and therapy.[30] Liu et al prepared magnetic-fluorescent dual-modality probes based on gadolinium-functionalized AIE dots for cancer metastasis studies.[31] Tong and her coworkers synthesized a novel tetraphenylethene (TPE) derivative containing Gd (TPE-2Gd). These contrast agents have AIE characteristics, excellent longitudinal relaxivity in water and a long circulation lifetime for high-resolution images.[32] Hu et al developed theranostic nanoparticles with MR/FL dual-modal imaging diagnostic and therapeutic functionalities by integrating TPE, DOTA (Gd) MR imaging contrast agents and camptothecin (CPT) in one system. After conjugating with tumor-targeting peptides, the theranostic nanoparticles showed better tumor accumulation and MR imaging performance.[33] It should be noted that many AIE dyes that have been used in MR/FL dual-modal probe systems are

blue or green emitters. These AIE dyes have limited tissue penetration depth and autofluorescence interference. To overcome these problems, AIE dye with emission in the near-infrared region has been used to develop near-infrared MR/FL dual-modal probes.[34] Furthermore, some AIE dyes have the ability to transfer the absorbed optical energy to molecular oxygen, generating ROS and singlet oxygen.[35,36] ROS can oxidize the surrounding biomolecules and induce cell death through apoptosis, necrosis and/or autophagy.[37] AIE dyes can be used as both fluorescent imaging probes and as photosensitizers for PDT.[38,39] Therefore, AIE-based theranostic nanoparticles with MR/FL dual-modal imaging characteristics show great potential in the field of image-guided PDT.

Herein, we developed MR/FL dual-modal imaging theranostic nanoparticles for targeted image-guided photothermal therapy. Amphiphilic hyaluronan acid/poly-(*N*-ε-carbobenzyloxy-L-lysine) derivatives were prepared through a click chemistry reaction. As Figure 1 illustrates, the obtained HA-*g*-PZLLs self-assembled into nanoparticles in aqueous solution, and SPIO and AIE could be loaded into the inner core of the nanocarrier, while the hydrophilic HA on the surface of the nanocarrier extended into the aqueous media, which could target CD44-overexpressing cancer cells. The obtained theranostic nanoparticles SPIO/AIE@HA-*g*-PZLL show high fluorescence efficiency and strong magnetization. Under white light irradiation, these theranostic nanoparticles can produce enough singlet oxygen for photodynamic tumor therapy. Moreover, the cellular uptake, intracellular ROS generation and photocytotoxicity of the theranostic nanoparticles against HepG2 cells were evaluated using CLSM, flow cytometry, Prussian blue staining and (methyl thiazolyl tetrazolium) MTT assays. Finally, theranostic nanoparticles were used for in vivo MR imaging of HepG2 cells in mice.

Materials and Methods

Materials

Hyaluronan acid with a molecular weight of 8.5 kDa, was obtained from C.P. Freda Pharmaceutical Co. Ltd. (Shangdong, China) as sodium salts. Tetrahydrofuran (THF, 99.5%) was refluxed and distilled over sodium benzophenone until a purple color was obtained. N-(3-Dimethylaminopropyl)-N′-ethylcarbodiimide hydrochloride (EDC), N-Hydroxysuccinimide (NHS), copper sulfate ($CuSO_4 \cdot 5H_2O$), sodium ascorbate (99%), triphosgene (98%), N-epsilon-benzyloxycarbonyl-L-lysine (ZLL) (98%) and propargylamine (98%) were purchased from Aldrich. MTT, dimethyl sulfoxide, paraformaldehyde and phosphate buffer solution (PBS; pH = 7.0) were purchased from Sigma-Aldrich Corporation, USA. Human hepatocellular carcinoma cell lines (HepG2) were obtained from ATCC. Dulbecco's modified Eagle's medium (DMEM), fetal bovine serum, pancreatin, phosphate buffer saline (PBS), penicillin and streptomycin were purchased from Guangzhou Zuoke Biotechnology Co. Ltd, China. 1-Azido-3-aminopropane was synthesized according to a reported procedure.

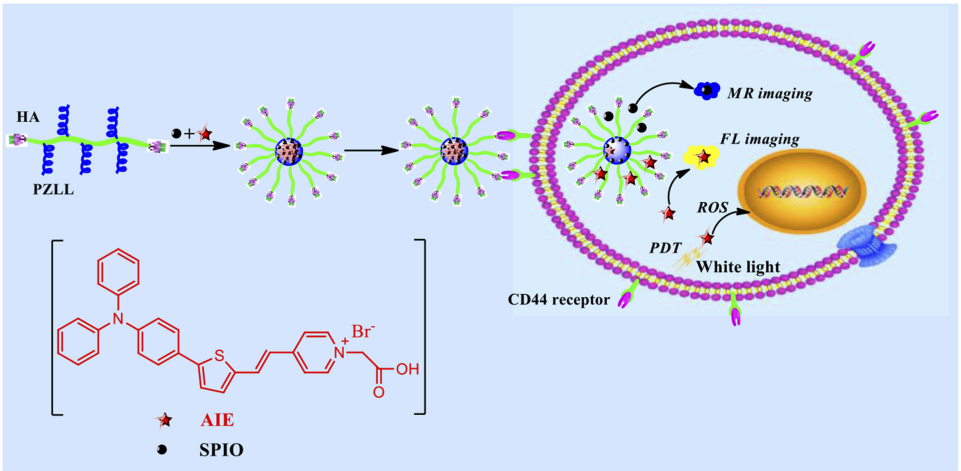

Figure 1 The preparation of dual-modal imaging platform for MR/FL image-guided tumor photodynamic therapy.
Abbreviations: HA, hyaluronan; PZLL, poly-(N-ε-carbobenzyloxy-L-lysine); SPIO, superparamagnetic iron oxide; AIE, aggregation-induced emission; MR, magnetic resonance; FL, fluorescence; PDT, photodynamic treatment; ROS, reactive oxygen species; CD44, cluster of differentiation 44.

Synthesis of Propargylamido-Substituted-HA (HA-PPA)

Propargylamido-substituted hyaluronan derivatives were prepared by a chemical conjugation method. Typically, HA (3 g, 0.20 mmol) was dissolved in 40 mL of deionized water. EDC (0.48 g, 2.5 mmol) and NHS (0.30 g, 2.5 mmol) were added under magnetic stirring for 2 h. Then, propargylamine (0.22 g, 2.5 mmol) was added, and the pH value of the solution was adjusted to 5.5 by adding 0.1 M HCl and the mixture was stirred at room temperature for 24 h. In order to obtain pure product, excess reagents were removed from the mixture by dialysis (MWCO =1 kDa) against water. The dialysate was lyophilized; thus, a white powder (2.74 g, 91%) was received. Fourier transform infrared spectroscopy (FTIR, KBr, cm^{-1}): 3200–3600 (ν N-H and ν O-H), 2883 (ν C-H), 1650 (ν C=O), 1110 (ν C-O). The degree of substitution (DS, the percent of carboxyl-derived azido groups) was calculated from the ^{1}H Nuclear magnetic resonance spectrum (NMR, Bruker, Germany, 500 MHz, D_2O) by integration of the methylene proton at 2.74 ppm belonging to 3-azidopropanamine compared to the N-acetyl methyl group signal located at 1.85 ppm. From the HA-N_3 ^{1}H-NMR spectrum, approximately 10% of the carboxyl groups of HA reacted with 3-azidopropanamine.

Synthesis of α-Azido-Poly-(*N*-ε-Carbobenzyloxy-L-Lysine)

The synthetic homo polypeptide, α-azido-poly-(*N*-ε-carbobenzyloxy-L-lysine) (N_3-PZLL) was synthesized using a well-studied N-carboxyanhydride (NCA) ring-opening polymerization (ROP) of Z-L-lysine-N-carboxyanhydride (ZLL-NCA) and 3-azidopropanamine as the initiator. First, ZLL-NCA was synthesized following an already published procedure. In brief, ZLL (4.2 g, 20 mmol) and triphosgene (2.0 g, 6.74 mmol) were suspended in 60 mL of dry THF bubbled with slow steady nitrogen flux in a flame-dried three-neck flask. The mixture was stirred in a 50°C oil bath until the cloudy solution turned clear. The mixture was concentrated by reduced pressure distillation, and a yellowish oil was obtained and dissolved in 100mL of ethyl acetate, followed by washing with 50 mL of 0.5% ice-cold aqueous $NaHCO_3$ solution three times. The organic phase was then dried over anhydrous $MgSO_4$ and evaporated to give ZLL-NCA as a white solid (3.4 g, 70%). Then, 10 of anhydrous N,N-Dimethylformamide (DMF) and ZLL-NCA (0.306 g, 1 mmol) was introduced into a dried Schlenk flask under an argon atmosphere with continuous stirring. 3-Azidopropanamine (0.024 g, 0.1 mmol) as the initiator was introduced into the reaction mixture, which was stirred for 3 days at room temperature. The mixture was placed into a dialysis bag and dialyzed in distilled water for 2 days to remove the DMF. The deposit was collected and dried under vacuum. ^{1}H NMR (yield=90%). ^{1}H NMR ($CDCl_3$/CF_3CO_2D (v/v) 85:15, δ, ppm): 1.24 (m, 2H, -CH$CH_2$$CH_2$-), 1.39 (m, 2H, -CH$CH_2$$CH_2$-), 1.7 (t, 2H, -CH$CH_2$CH2-), 3.09 (2H, -NHC$H_2$$CH_2$), 3.95 (2H, -C$CH_2$NH-) 4.41 (s, 1H, -NH$CH$), 5.08 (s, 2H, -OC$H_2$Ph), 7.30 (s, 5H -Ph), 8.27 (s, 1H, -CONH-). FT-IR (KBr, cm-1): 3293 (ν N-H); 2944 (ν C-H), 1734 (ν CO-O), 1652 (ν C=O), 1546, 1386 (ν CO-NH).

Synthesis of HA-*g*-PZLL by a Huisgen's 1,3-Dipolar Cycloaddition

The process for Huisgen's 1, 3-dipolar cycloaddition (click reaction) was that HA-PPA (0.685g, 40 μmol, 1 equiv) and α-azido-PZLL (0.6 g, 50 μmol, 1.25 equiv) were dissolved in 20 mL of DMSO with argon bubbling. After the HA-PPA and the PZLL dissolved completely, 10 mg of $CuSO_4.5H_2O$ was introduced into the flask and the mixture was further bubbled with argon for approximately 5 min until 16 mg of sodium ascorbate (NaAsc) was added. The Schlenk flask was sealed and placed in an oil bath regulated at 60°C for 2 days. The excess HA-PPA was removed by extensive dialysis (MWCO=50 kDa) against water for 3 days. After dialysis and lyophilization, the block copolymers were obtained as a white powder (0.9 g, 77%).

Preparation of Blank Nanoparticles

Dialysis is an easy way to self-assemble the amphiphilic copolymer in water. HA-*g*-PZLL copolymer (10 mg) was dissolved in 2mL of dimethyl sulfoxide (DMSO) and then dialyzed in 25°C deionized water for 24 h in a cellulose membrane bag with a molecular weight cut-off of 3.5 kDa. The solution was filtered through a 0.45 μm syringe filter and analyzed by dynamic light scattering (DLS) and transmission electron microscopy (TEM).

Preparation of SPIO/AIE-Loaded Theranostic Nanoparticles

Tumor-targeting multifunctional nanoparticles simultaneously loaded with AIE and SPIO were developed for targeted cancer photodynamic therapy and FL/MR dual-modal imaging. In brief, 2 mL of warm DMSO containing AIE (1 mg), SPIO (1 mg) and grafted copolymer (10 mg)

was added dropwise into 5 mL of PBS (pH=7.5) under vigorous stirring. The resulting mixture solution was transferred into a dialysis bag (MWCO= 3.5 kDa) and dialyzed against water to remove the unencapsulated AIE and SPIO and excess DMSO was removed by dialysis for 24 h against PBS (MWCO= 3.5 kDa). Finally, the mixture solution was filtered through 0.45 μm syringe filter membrane. The AIE loading content (LC) and loading efficiency (LE) were determined by a Ultraviolet–visible spectrophotometer (UV-Vis) at 497 nm. The AIE loading content was determined as follows: the SPIO/AIE@HA-g-PZLL nanoparticles were broken in a mixture (DMSO: PBS (v: v= 90:10)). Then, the sample was filtered and subjected to UV analysis at λ max of 497 nm. Quantification was carried out from the calibration curve of AIE in the DMSO: PBS (v: v= 90:10) mixture. The AIE loading content (LC) and loading efficiency (LE) were calculated from the following equations:

$$LC(\%) = w_1/w_2 \times 100 \quad (1)$$

$$LE(\%) = w_1/w_3 \times 100 \quad (2)$$

where w_1 is the weight of loaded AIE, w_2 is the weight of HA-*g*-PZLL, and w_3 is the weight of AIE in the feed.

The SPIO loading content was determined from atomic absorption spectroscopy (AAS) at 248.3 nm, a specific absorption wavelength for Fe, based on a previously established calibration curve.

Characterization

FTIR spectra of all samples were obtained in transmission mode on a Perkin-Elmer Paragon 1000 spectrometer under ambient conditions. Samples were ground with KBr and then compressed into pellets. The spectra were taken at frequencies ranging from 500 to 4000 cm^{-1}. Typically, 32 scans at a resolution of 8 cm^{-1} were accumulated to obtain one spectrum. ^1H NMR spectra measurements were performed on a Bruker 500 NMR spectrometer operating at 500 MHz using deuterated chloroform ($CDCl_3$-*d*) or deuterated dimethyl sulfoxide (DMSO-d_6) as the solvent and tetramethylsilane (TMS) as the internal standard. The temperature was 25°C. The mean particle size and distribution of all samples were measured in water (pH 7.4) using a dynamic/static laser scattering system (BI-200SM, Brookhaven Instruments Corporation). The dialyzation solutions were filtered through 0.45 μm pore size filters, the measurements were conducted using a 630 nm diode laser at 25°C, and the scattering angle was fixed at 90°. The presented data are the means of three independent measurements. The morphology of the block polymer was observed using TEM. Briefly, one drop of the micelle solution was placed on a copper grid. Excess liquid was removed by blotting with filter paper. The sample was negatively stained with 2% (w/v) phosphotungstic acid solution for 60 s and again blotted dry with filter paper. TEM images were recorded with a transmission electron microscope (JEM2010) operated at 80 kV.

Cell Culture

HepG2 cells were cultured in a regular growth medium composed of Dulbecco's modified Eagle's medium supplemented with 10% fetal bovine serum and 1% penicillin/streptomycin at 37°C in a humidified environment containing 5% CO_2.

Cellular Uptake

HepG2 cells were separately seeded on 24-well plates at a density of 1×10^5 cells/well and cultured for 24 h to achieve the logarithmic growth phase. Then, 500 μL of SPIO/AIE@HA-g-PZLL nanoparticle solution at four different concentrations (0 μg/mL, 0.1 μg/mL, 0.5 μg/mL, 1 μg/mL) was added to each well of the 24-well plates, with each concentration having four duplicates, and then the cells were incubated for 24 h. Next, the mixture medium in each well was removed by pipetting, and the cells were washed twice with PBS, and observed under an Olympus 1X71 fluorescence microscope.

Furthermore, the dynamic uptake process according to time and the blocking experiment were carried out. HepG2 cells were incubated with SPIO/AIE@HA-g-PZLL nanoparticle solution (AIE concentration of 1 μg/mL) for 1 h, 4 h and 12 h in several confocal cell incubators. After staining the cell nuclei with Hochest 33258, the cells were evaluated by CLSM. In the blocking experiment, the HepG2 cells were first incubated with free hyaluronic acid (Mw=8.5 kDa) at a concentration of 2 mg/mL at 37°C or 8 h, and then the HepG2 cells were washed twice with PBS and incubated with SPIO/AIE@HA-g-PZLL nanoparticle solution (AIE concentration of 1 μg/mL) for 4 h. After staining the cell nuclei with Hochest 33258, the cells were evaluated by CLSM.

Cellular uptake was quantitatively investigated by flow cytometry (Guava easyCyte 5HT-2L, Merck Millipore, Germany). HepG2 cells were seeded on 6-well plates at a density of 2×10^5 cells/well and incubated overnight. After the cells attached, the culture medium was removed,

and the cells were incubated with SPIO/AIE@HA-g-PZLL nanoparticle solutions at different AIE concentrations (0, 0.1, 0.5 and 1 μg/mL). After 24 h of incubation, 200 μL of a solution containing 0.25% EDTA was injected into each well to digest the cells for 3 min, and the cells were collected in a flow tube and washed three times with PBS. After the cell number in each tube was confirmed to be more than 1×10^6 cells, the cellular uptake e□ciency was determined by flow cytometry.

Prussian blue staining was carried out to suggest the uptake of the SPIO/AIE@HA-g-PZLL nanoparticle solution by HepG2 cells. In total, 2×10^5 HepG2 cells were seeded in a 12-well plate for 24 h. Then, the SPIO/AIE@HA-g-PZLL nanoparticle solution (final concentration of iron was 10, 5, 2.5 and 1.25 mM) was added followed by cultivation at 37°C for 12 h. The cells were washed three times with PBS and fixed with 4% formaldehyde for 10 min. The fixed cells were incubated with 500 μL of pre-prepared Prussian blue solution at 37°C for 30 min, and then washed three times with PBS. Iron staining of the cells was observed under a microscope.

Intracellular ROS Detection

ROS production inside the cells after light irradiation was detected using the ROS-sensitive probe dichlorofluorescein diacetate (DCF-DA). After reaction with ROS, DCF-DA can form DCF, which emits green fluorescence, and CLSM and flow cytometry were used to evaluate the effect of ROS generation. For CLSM, HepG2 cells were seeded onto 15 mm glass-bottom dishes at a density of 1×10^4. After the cells were attached and the cell density reached 70%-80%, the culture medium was removed. Then, the HepG2 cells were incubated with the SPIO/AIE@HA-g-PZLL nanoparticle solution (AIE concentration of 2 μg/mL) for 4 h and washed twice with PBS. Second, the cells were incubated with 5 μg/mL DCFH-DA in DMEM for 20 min and then exposed to light irradiation at a power density of 10 mW/cm^2 for 0, 5 or 10 min. Then, the cells were fixed with 4% paraformaldehyde for 10 min and washed with PBS three times, and the nuclei was stained with Hoechst 33342 (1:1000) for 5 min followed by washing with PBS three times. Cells were observed under a laser confocal microscope (Nikon, Japan). For flow cytometry analysis, HepG2 cells (1×10^6) were seeded in a 6-well culture plate and cultured for 24 h to achieve logarithmic growth of the cells. After the culture medium was removed, the cells were incubated with SPIO/AIE@HA-g-PZLL nanoparticle solution (AIE concentration of 2 μg/mL) for 4 h and washed twice with PBS. Then, culture medium containing 5 μg/mL DCFH-DA was added to the culture medium and incubated for 20 min, followed by exposure to light irradiation at a power density of 10 mW/cm^2 for 0, 5 or 10 min. The culture medium was removed. The cells were treated with trypsin, centrifuged, washed with PBS three times, and resuspended in 0.3 mL of PBS. At least 10,000 cells were analyzed from each sample.

Photodynamic Therapy

The experimental procedure is described in the following steps. First, HepG2 cells were seeded in a 96-well plate at a density of 1×10^5 cells/well and incubated for 24 h. Then, the SPIO/AIE@HA-g-PZLL nanoparticle solution (AIE concentration of 0.25 μg/mL, 0.5 μg/mL, 1 μg/mL, 2 μg/mL, 4 μg/mL or 8 μg/mL) was added to the culture media except the blank control and incubated for 12 h. Second, the 96-well plate was irradiated by white light at a power density of 10 mW/cm^2 for 10 min, and the HepG2 cells were incubated in the dark for 24 h. The irradiated cells were used as test samples, whereas the cells in the wells without irradiation were used as control samples. Thereafter, the wells were washed three times with PBS, and then 10 μL of the MTT reagent (5 mg/mL in PBS) was separately added to the test and control samples. All the cells were continuously incubated for 4 h at 37°C, allowing viable cells to reduce the yellow MTT to dark blue formazan crystals. After the mixed solutions were pipetted from the 96-well plate, 100 μL of DMSO was added to each well to dissolve the formazan crystals. Then, the 96-well plate was shaken on a swing bed for 10 min at 37°C. Finally, the absorbance of the solution in each well was measured with a microplate reader (TECAN NanoQuant plate Infinite 200 Pro) at 570 nm to evaluate the viability of the HepG2 cells.

Ability of the in vitro Dual-Modal Imaging

The application of the dual-modal imaging of SPIO/AIE@HA-*g*-PZLL nanoparticles was performed using T_2-negative enhanced MR imaging and fluorescence imaging in vitro. For MR imaging, the iron concentration was diluted to 0.5 mM, 0.25 mM, 0.125 mM, 0.0625 mM and 0.0312 mM with deionized water and imaged using a 3.0 Tesla MR imaging scanner (Verio, Siemens, Erlangen, Germany) with an 11 cm circular surface coil. T_2-weighted images were acquired using the following parameters: TR/TE 5000/100 ms; FOV 150 mm; matrix, 256 × 256; and slice thickness 1.5 mm. T_2 signal intensities were measured using the region

of interest technique. For in vitro FL imaging, 100 μL of SPIO/AIE@HA-*g*-PZLL nanoparticle solution (AIE concentration of 1.56, 3.125, 6.25 or 12.5 μg/mL) was added to a 96-well plate, and PBS was used as the blank control. Then, the 96-well plate was exposed to an FLI machine. The scan parameters were as follows: excitation laser was 490 nm, emission wavelength was 600 nm, and the scan time was 6 s.

In vivo MR Imaging

All animal experiments were approved by the Medical Ethics Committee of South China University of Technology. All of the animal studies were conducted in compliance with guidelines set by the Animal Care Committee at South China University of Technology. To establish the tumor-bearing mouse model, HepG2 cells (2×10^6) dispersed in 100 μL of PBS were subcutaneously inoculated into the right front flank of female BALB/c nude mice, and the tumor volume was calculated using the following formula: volume = ((tumor length) × (tumor width)^2)/2. When the tumor nodules reached the expected size (approximately 200–300 mm^3), the mice were used for experiments. For in vivo MR imaging, 3.0 T MR imaging scanner equipped with a soft coil was used at room temperature. Tumor-bearing mice were imaged using a spin echo sequence (TR =3500 ms, TE =88 ms). MR images were recorded before and after tail vein injection of SPIO/AIE@HA-*g*-PZLL nanoparticle solution (5 mg/kg Fe of body weight) at various time points (0, 2 and 8 h).

Results and Discussion

Synthesis of HA-*g*-PZLL

The grafted copolymer HA-*g*-PZLL was synthesized via click chemistry conjugation. To this aim, hydrophobic PZLL with an azido terminal group was prepared through ring open polymerization (ROP) of the ZLL-NCA monomer and 3-azidopropanamine as the initiator, as shown in Figure 2. The ROP reaction was carried out in anhydrous DMF at room temperature for 3 days. After purification, N_3-PZLL was obtained as white solid, and the chemical structure of PZLL was characterized by FTIR and ^{1}H NMR. The characteristic absorption peak of the azido group was located at 2100 cm^{-}1.[40] As seen from the data in Figure 3A, a characteristic absorption peak appeared at 2103 cm^{-1}, which belongs to the azido group. Furthermore, the characteristic peak located at 3300 cm^{-1} was attributed to the *N-H* absorption peak, the peak at 2950 cm^{-1} was attributed to C-H, and the absorption peak of the C=O group was located at 1748 cm^{-1}. The ^{1}H NMR spectrum of N_3-PZLL with peak assignments is shown in Figure 4A. As expected, all peaks appeared in the ^{1}H NMR spectrum. In particular, from the ^{1}H NMR spectrum, we found that the methylene protons belonging to the initiator (NH_2CH_2-$CH_2CH_2N_3$) were observed at 3.3, 0.85 and 2.1 ppm, respectively. Furthermore, the molar mass of PZLL was approximately 35, which could be calculated by the relative integration of the methylene group signal at 1.78 ppm (-$CH_2CH_2CH_2N_3$) compared to the methylene proton signal of the benzylic groups located at 5.0 ppm (-O-CH_2-Ph).[41] Propargyl amido-substituted hyaluronan was prepared in the presence of EDC/NHS to activate the carboxyl groups of HA, and then the activated HA was reacted with propargylamine under continuous stirring for 24 h. The FTIR analysis for HA-PPA is shown in Figure 3B. The characteristic peak for the -OH group was located at 3500 cm^{-1}, and a C=O stretching band appeared at 1652 cm^{-1}. Figure 4B shows the ^{1}H NMR HA-PPA proton signals. The diastereotopic proton signals at 4.0 and 4.1 ppm belonged to the methylene group (-NH-CH_2-C≡CH) of propargylamine, which indicated that propargyl amido-substituted hyaluronan was prepared. HA-*g*-PZLL was prepared via the "azido-alkylene" click conjugation reaction. From Figure 3C we found that the characteristic peak at 2103 cm^{-1} belonging to the azido group disappeared, and the absorption peaks at 3300 and 1748 cm^{-1} were assigned to the presence of the -NH and C=O groups on the PZLL backbone, and the -OH group absorption band for the HA block was at 3500 cm^{-1}. The above result could confirm completion of the click conjugation reaction. Furthermore, the ^{1}H NMR spectrum of HA-*g*-PZLL is illustrated in Figure 5. The ^{1}H NMR spectrum not only clearly shows the typical proton signals of both the PZLL and HA blocks, but also shows that the proton signal peak of triazole ring appeared at 7.5 ppm.[17] These data enable us to conclude that the HA-*g*-PZLL grafted copolymer was prepared through the click conjugation reaction.

Self-Assembly Behavior of HA-*g*-PZLL

Owing to their good biocompatibility, water solubility and tumor-targeting ability, HA is regarded as an attractive candidate in the field of biomaterials.[42] In this work, click chemistry, a versatile chemical modification methodology, was used to graft a hydrophobic block PZLL onto the HA backbone. The obtained HA derivatives show amphiphilic properties and are expected to self-assemble into nanoparticles such as micelles in aqueous solution. The critical micelle concentration (CMC) is an important

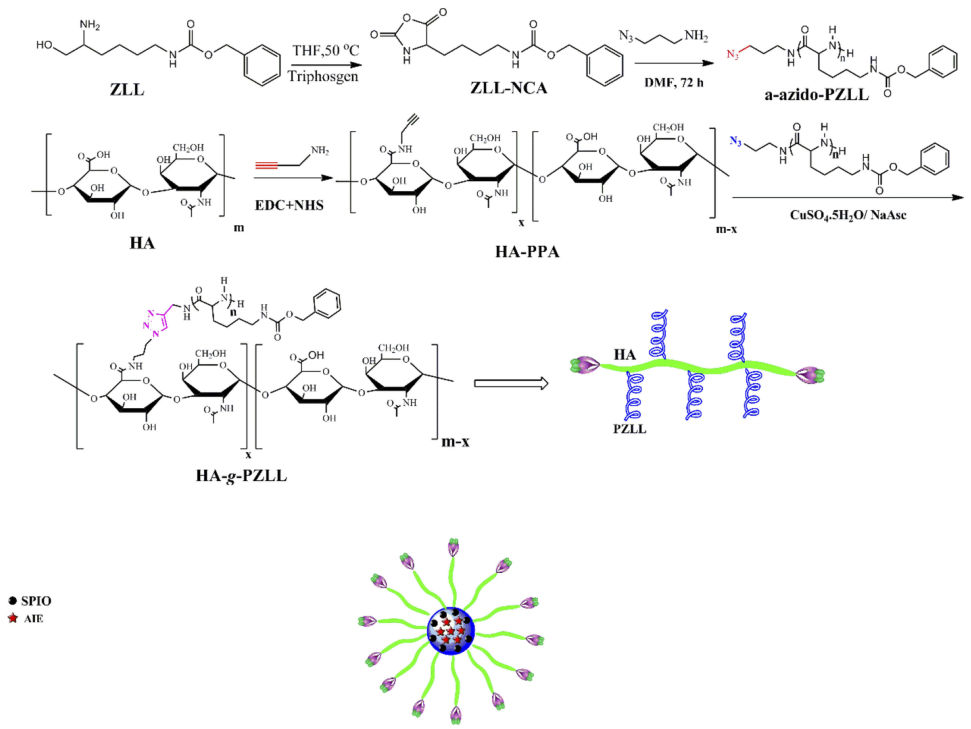

Figure 2 Synthetic routes for the preparation of amphiphilic hyaluronan derivatives HA-*g*-PZLL.
Abbreviations: ZLL, N-epsilon-benzyloxycarbonyl-L-lysine; THF, tetrahydrofuran; ZLL-NCA, Z-L-lysine-N-carboxyanhydride; DMF, N,N-dimethylformamide; PZLL, poly-(N-ε-carbobenzyloxy-L-lysine); HA, hyaluronan; EDC, N-(3-dimethylaminopropyl)-N′-ethylcarbodiimide hydrochloride; NHS, N-hydroxysuccinimide; PPA, propargylamine; SPIO, superparamagnetic iron oxide; AIE, aggregation-induced emission; m-x, degree of polymerization of HA; m, degree of polymerization of HA; x, degree of polymerization of HA-*g*-PZLL; HA-*g*-PZLL, hyaluronan/poly-(N-ε-carbobenzyloxy-L-lysine) derivative.

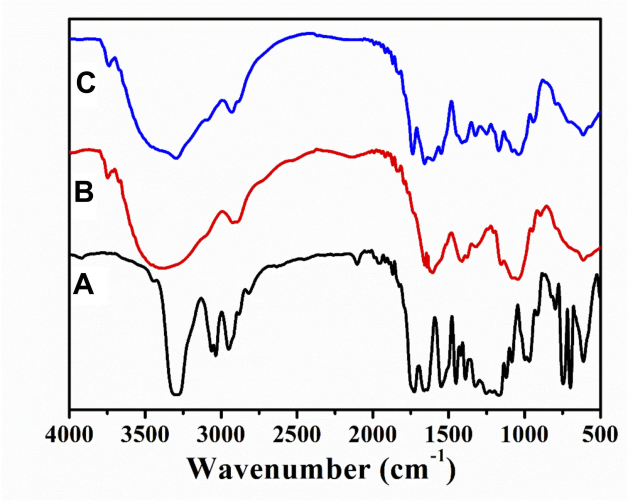

Figure 3 FTIR spectral of (**A**) N_3-PZLL, (**B**) HA-PPA and (**C**) HA-*g*-PZLL.
Abbreviations: FTIR, Fourier transform infrared spectroscopy; N_3-PZLL, α-azido-poly-(N-ε-carbobenzyloxy-L-lysine); HA-*g*-PZLL, hyaluronan/poly-(N-ε-carbobenzyloxy-L-lysine) derivative; HA-PPA, propargylamido-substituted hyaluronan.

parameter that reflects the formation and thermodynamic stability of micelles in aqueous and can be determined by using a pyrene fluorescence probe.[43] Figure 6A shows the emission spectra for the pyrene-loaded HA-*g*-PZLL solutions. From the emission spectra, we found that the wavelength for the absorbance peak of the pyrene probe was nearly constant below a certain concentration. As the concentration increased substantially, an obvious redshift occurred, which indicated the incorporation of pyrene into the hydrophobic domain formed by HA-*g*-PZLL. The CMC value was calculated from Figure 6B by the ratio of the pyrene fluorescence intensities at 337 and 335 nm (I_{337}/I_{335}) against the logarithm of the copolymer concentrations. The CMC value was approximately 0.0733 mg/mL, which indicated that HA-*g*-PZLL could form stable nanostructures in aqueous solution.

Then, the size and morphology of the nanoparticle solutions at a constant copolymer concentration of 1.0 mg/mL was revealed by dynamic light scattering (DLS) measurements at 90° and transmission electron microscopy (TEM) analysis negatively stained with 1.5% phosphotungstic acid solution. As illustrated in Figure 7A, a monomodal size distribution was observed, and the average size for the nanoparticles was approximately 100 nm. The morphology of the nanoparticles was revealed by TEM, as shown in Figure 7B, in which monodispersed well-defined spherical HA-g-PZLL nanoparticles were observed. We found that the average

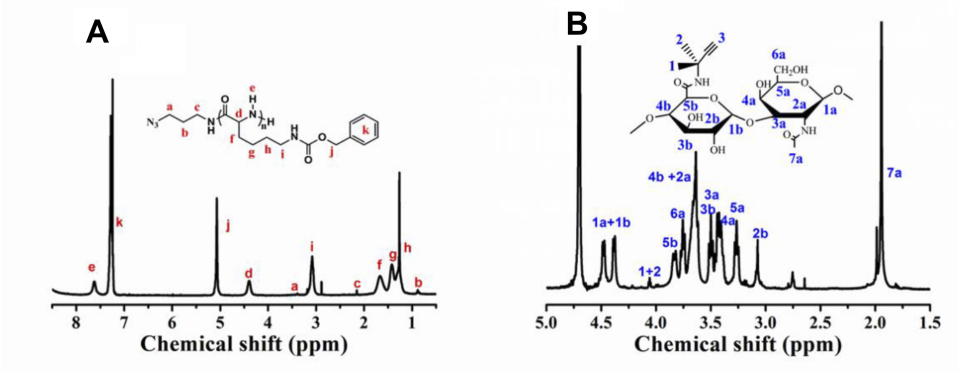

Figure 4 (**A**) ^{1}H NMR spectral of N_3-PZLL in $CDCl_3$-*d* contain 15% Trifluoroacetic Acid (TFA), (**B**) ^{1}H NMR spectral of (**B**) HA-PPA in D_2O-*d*.
Abbreviations: NMR, nuclear magnetic resonance; N_3-PZLL, α-azido-poly-(N-ε-carbobenzyloxy-L-lysine); $CDCl_3$-*d*, deuterium chloroform; HA-PPA, propargylamido-substituted hyaluronan; D_2O-*d*, deuterium oxide.

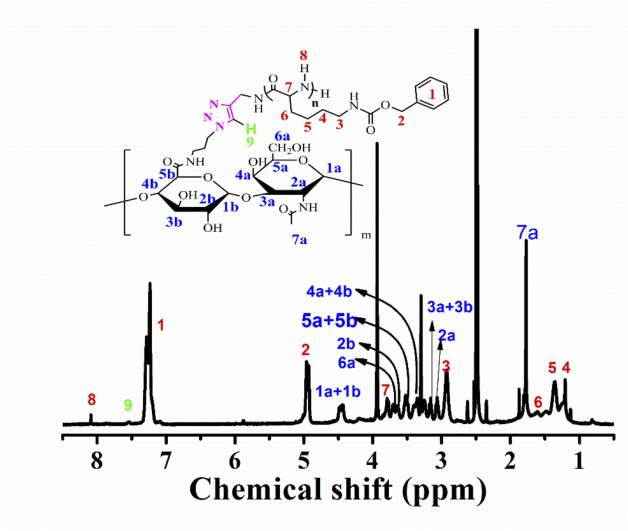

Figure 5 ^{1}H NMR spectrum of HA-*g*-PZLL in DMSO-*d6*.
Abbreviations: NMR, nuclear magnetic resonance; DMSO-*d6*, deuterium dimethylsulfoxide; HA-*g*-PZLL, hyaluronan/poly-(N-ε-carbobenzyloxy-L-lysine) derivative.

particle size detected by TEM was approximately 70 nm, which is smaller than the DLS results.

Synthesis and Characteristics of the SPIO/AIE@HA-g-PZLL Nanoparticles

Nanoparticles play an important role in the field of nanomedicine. In this work, hydrophobic SPIO nanoparticles and the dye AIE were encapsulated into the inner domain of the nanoparticles through a dialysis method. It has been reported that after loading with hydrophobic guest molecules, the nanoparticles show an increase in diameter.[44] As illustrated in Figure 7C, the mean diameter of the SPIO/AIE@HA-*g*-PZLL nanoparticles obtained from DLS measurements was approximately 184 nm. The increase in diameter may be due to AIE and SPIO loading into the nanoparticles. As shown in Figure 7D, the TEM images of SPIO/AIE@HA-*g*-PZLL nanoparticles show well-defined spherical shapes, and the mean diameter was larger than that of the blank HA-*g*-PZLL nanoparticles.

The photophysical properties of SPIO/AIE-loaded nanoparticles were examined by UV-vis and Photoluminescence (PL) spectroscopy and are illustrated in Figure 8A. As the UV-vis spectra show, a maximum absorption peak belonging to the SPIO/AIE@HA-*g*-PZLL nanoparticles appeared at 459 nm. PL spectra were recorded under 459 nm excitation. In the PL spectra, an emission peak appeared at 615 nm, and the SPIO/AIE@HA-*g*-PZLL nanoparticles showed a typical AIE effect, which clearly indicated that the AIE monomers were encapsulated into the hydrophobic inner core without fluorescence quenching. Furthermore, a large Stokes shift (156 nm) of the AIE/SPIO-loaded nanoparticles showed great potential in the field of bioimaging applications.[34,45] Then, in vitro bioimaging experiments were performed to investigate the FL imaging ability of the SPIO/AIE@HA-*g*-PZLL nanoparticles. As shown in Figure 8B, as the AIE concentration increased, a strong fluorescence imaging signal showing an excellent signal-to-noise ratio was obtained. These results suggest the potential of subcellular fluorescence bioimaging in vitro.

The generation of reactive oxygen species plays an important role in PDT. Previous studies have shown that ROS can oxidize anthracene in 9, 10-anthracene-bis (methylene) dimalonic acid (ABDA), resulting in a rapid decrease in the ultraviolet absorption spectra.[46] ROS production from the SPIO/AIE@HA-*g*-PZLL nanoparticles

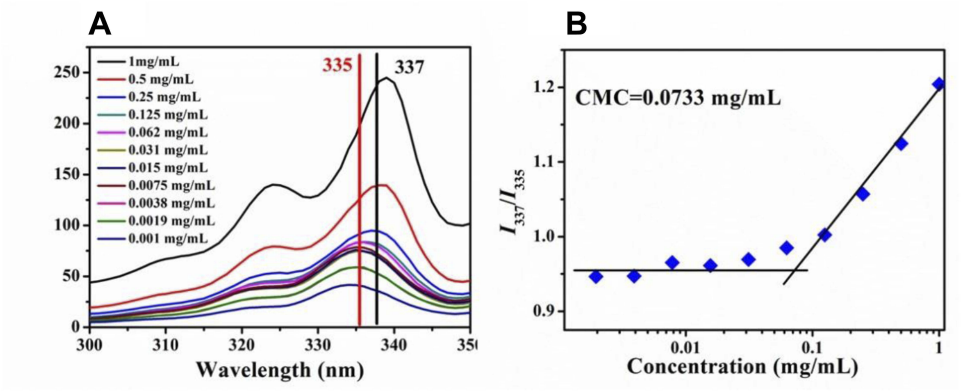

Figure 6 (**A**) Emission spectral for the pyrene-loaded HA-*g*-PZLL solutions. (**B**) Plot of I_{337}/I_{335} in the excitation spectrum versus the concentrations of copolymers in aqueous solution.
Abbreviations: HA-*g*-PZLL, hyaluronan/poly-(N-ε-carbobenzyloxy-L-lysine) derivative; CMC, critical micelle concentration.

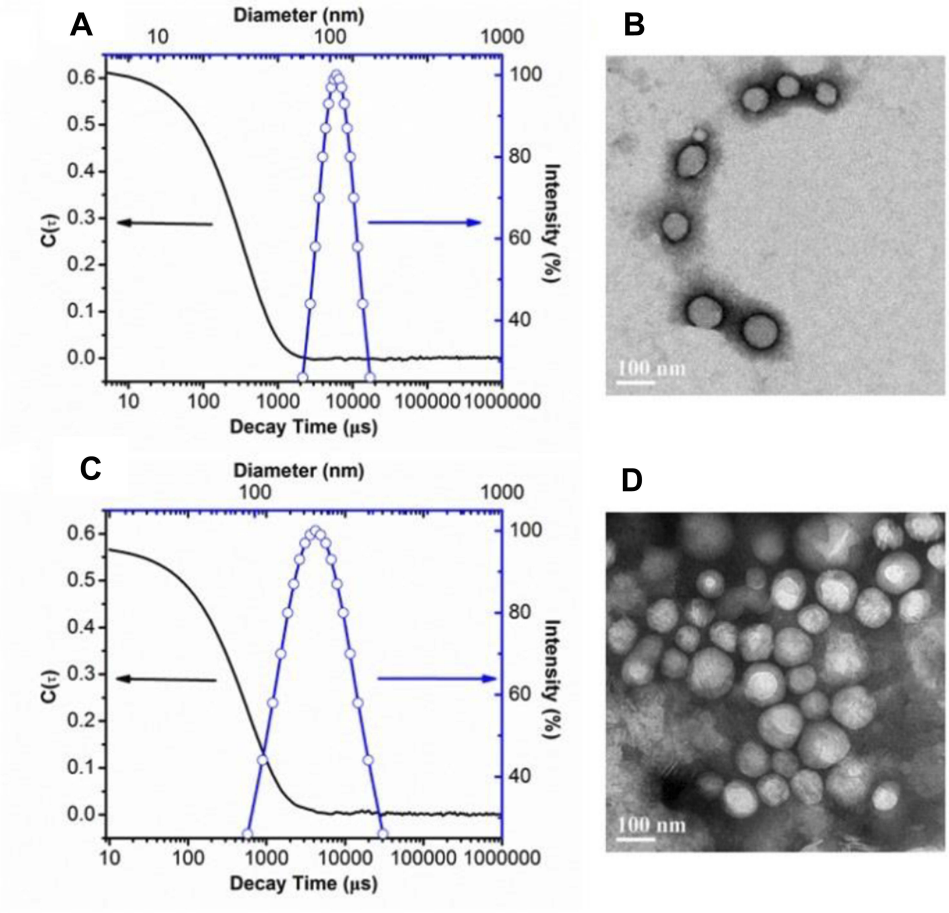

Figure 7 (**A**) Autocorrelation function and diameter distribution for HA-*g*-PZLL. (**B**) TEM image of HA-*g*-PZLL nanoparticles solution negatively stained with 1.5% phosphotungstic acid solution. (**C**) Autocorrelation function and diameter distribution for SPIO/AIE@HA-*g*-PZLL. (**D**) TEM image of SPIO/AIE@HA-*g*-PZLL nanoparticles solution negatively stained with 1.5% phosphotungstic acid solution.
Abbreviations: HA-*g*-PZLL, hyaluronan/poly-(N-ε-carbobenzyloxy-L-lysine) derivative; C(t), autocorrelation function; TEM, transmission electron microscope; SPIO, superparamagnetic iron oxide; AIE, aggregation-induced emission.

can be measured by the UV absorption spectra of ABDA as an indicator of ROS. As shown in Figure 8C, the UV absorption spectra of ABDA in the presence of SPIO/AIE@HA-*g*-PZLL nanoparticles at different illumination times were recorded. We should note that with white light irradiation (10mW/cm^2), the absorption peak of ABDA at

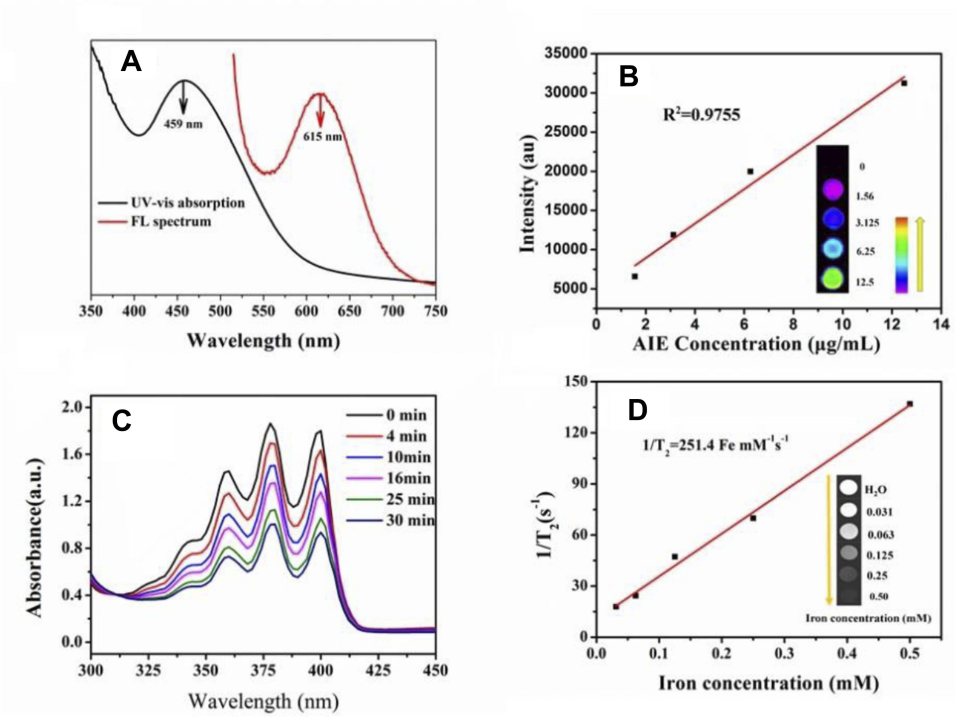

Figure 8 (**A**) Normalized UV-vis absorption and FL spectra of SPIO/AIE@HA-*g*-PZLL nanoparticles. (**B**) FL images of SPIO/AIE@HA-*g*-PZLL nanoparticles as a function of AIE concentration. (**C**) UV-vis absorbance changes of ROS indicator ABDA (200 mM) mixed with SPIO/AIE@HA-*g*-PZLL nanoparticles for different white light irradiation times. (**D**) Relaxation rate ($1/T_2$) and T_2-weighted MR images of SPIO/AIE@HA-*g*-PZLL nanoparticles as a function of iron concentration.

Abbreviations: HA-*g*-PZLL, hyaluronan/poly-(N-ε-carbobenzyloxy-L-lysine) derivative; UV-vis, ultraviolet-visible; FL, fluorescence; SPIO, superparamagnetic iron oxide; AIE, aggregation-induced emission; ROS, reactive oxygen species; ABDA, 9, 10-anthracene-bis (methylene) dimalonic acid; MR, magnetic resonance.

358, 378 and 400 nm decreases gradually, which confirms that the SPIO/AIE@HA-*g*-PZLL nanoparticles produce ROS.[45]

As a noninvasive diagnostic tool, MR imaging plays an important role in clinical diagnosis. In recent years, the development of MR/FL dual-modal imaging technology has received considerable attention, because imaging technology combines the advantages of tissue penetration depth, spatial resolution and sensitivity.[6,31] The MR imaging ability of SPIO/AIE@HA-*g*-PZLL nanoparticles was measured by a 3.0 T Siemens MRI scanner at room temperature. Figure 8D shows the T_2-weighted images. From these images, we can see that the higher the iron concentration, the darker the image. The results show that SPIO/AIE@HA-*g*-PZLL nanoparticles have negative contrast enhancement ability. The transverse relaxation time calculated from the T_2 rate of iron concentration is approximately 251.4 Fe $mM^{-1}s^{-1}$. Compared with Feridex® (111.5 Fe mM^{-1} s^{-1}), SPIO/AIE@HA-*g*-PZLL nanoparticles exhibit greater relaxation properties, indicating their potential in MR imaging.[47]

In vitro Cellular Uptake

The in vitro cellular uptake of SPIO/AIE@HA-*g*-PZLL nanoparticles were observed under a fluorescence microscope. As shown in Figure 9A, the control group did not show any red fluorescence, while cells treated with the nanoparticle solution showed red fluorescence, and the cells incubated with higher concentrations of AIE showed a higher fluorescence intensity. Fluorescence imaging results showed that even at a low AIE concentration (1 μg/mL), the cells still showed bright fluorescence, indicating that SPIO/AIE@HA-*g*-PZLL nanoparticles can be used as fluorescence probes for fluorescence imaging. The cellular uptake of SPIO/AIE@HA-*g*-PZLL nanoparticles was quantitatively analyzed by flow cytometry. As shown in Figure 9B, the corresponding fluorescence intensity curve shifted to the right after incubation of the cells with a high concentration of AIE. The above results showed that the fluorescence intensity of HepG2 cells was positively correlated with the concentration of AIE.

Cellular uptake of AIE at different time periods was studied by CLSM. As shown in Figure 9C, the fluorescence intensity of AIE in the cell increased gradually with

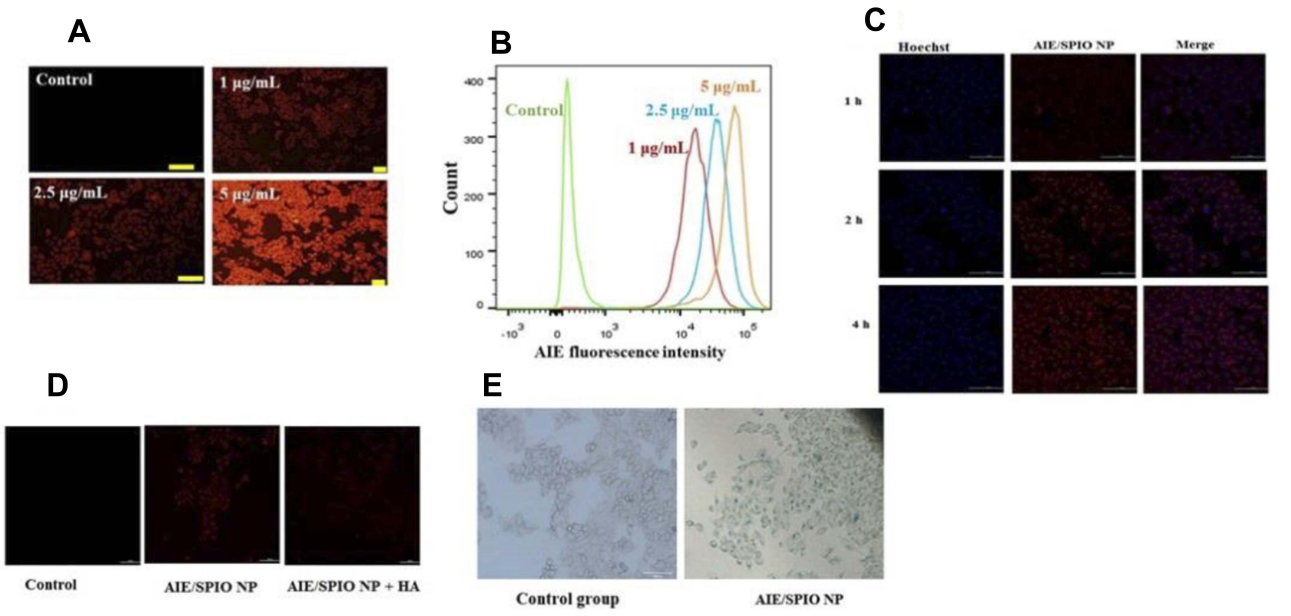

Figure 9 (**A**) Fluorescent images of HepG2 cells incubation with SPIO/AIE@HA-*g*-PZLL nanoparticles (AIE concentration: 0, 1, 2.5 and 5 μg/mL) for 12 h. Scale bars is 200μm. (**B**) Quantitative analysis of AIE fluorescence intensity in HepG2 cells after incubation with SPIO/AIE@HA-*g*-PZLL nanoparticles for 12 h. (**C**) CLSM images of HepG2 cells incubated with SPIO/AIE@HA-*g*-PZLL nanoparticles at 37°C. Scale bars is 200 μm. (**D**) Competitive inhibition of SPIO/AIE@HA-*g*-PZLL nanoparticles in the presence of free hyaluronan. Scale bars is 200 μm. (**E**) Prussian blue staining images of HepG2 cells incubated with SPIO/AIE@HA-*g*-PZLL nanoparticles (SPIO mM) for 4 h at 37°C. Scale bars is 200 μm.

Abbreviations: HA-*g*-PZLL, hyaluronan/poly-(N-ε-carbobenzyloxy-L-lysine) derivative; SPIO, superparamagnetic iron oxide; AIE, aggregation-induced emission; NP, nanoparticles; CLSM, confocal laser scanning microscopy.

increasing incubation time from 1, 2 to 4 h. In addition, the blue fluorescence in the nucleus was due to Hoechst; hence, from the merged CLSM, we found that AIE was predominately present in the cytoplasm of HepG2 cells.

ROS produced by photosensitizers under radiation exposure can oxidize a variety of cell molecules, resulting in cell death.[48] To avoid unnecessary damage to healthy tissues, tumor-specific nanoparticles based on amphiphilic HA derivatives were developed to enhance the accumulation of AIE in target tumors. The cellular uptake mechanism of the nanoparticles was revealed by competitive inhibition experiments. To block the HA receptor (CD44), HepG2 cells were treated with free HA. As shown in the CLSM image in Figure 9D, HepG2 cells without free HA showed bright red fluorescence, while the intracellular fluorescence intensity decreased significantly after treatment with free HA. We believe that the interaction between HA and the receptor (CD44) plays a key role in the cellular uptake of SPIO/AIE@HA-*g*-PZLL nanoparticles.[49]

Next, Prussian blue staining was performed to further prove the in vitro cellular uptake of SPIO/AIE@HA-*g*-PZLL nanoparticles. As shown in Figure 9E, blue spots were not detected in HepG2 cells incubated in pure medium, but obvious blue spots were detected in cells treated with SPIO/AIE@HA-*g*-PZLL nanoparticles. These results confirm that SPIO particles were efficiently taken into HepG2 cells.

Intracellular ROS Generation and PDT

The main pathways of cell death caused by ROS include apoptosis, necrosis and/or autophagy.[48] Therefore, the ROS generation ability of AIE-loaded nanoparticles under irradiation plays a key role in PDT. In this work, the ROS generation ability was measured by CLSM and flow cytometry, and dichlorofluorescein diacetate (DCF-DA) was used as a ROS-sensitive probe. As shown in Figure 10A, HepG2 cells without white light irradiation did not show green fluorescence, which indicated no ROS generation. The cellular uptake experiment confirmed that AIE molecules mainly accumulated in the cytoplasm. Once the cells were exposed to white light, the DCF-DA probe was oxidized to dichlorofluorescein (DCF) by ROS, and green fluorescence was detected in the cytoplasm. In addition, the intensity of green fluorescence in the cytoplasm increased gradually with increasing irradiation time from 5 min to 10 min, indicating that the AIE-loaded nanoparticles can effectively produce ROS under the complexity of biological system.

Figure 10B shows the flow cytometry quantitative analysis of DCF green fluorescence from HepG2 cells incubated

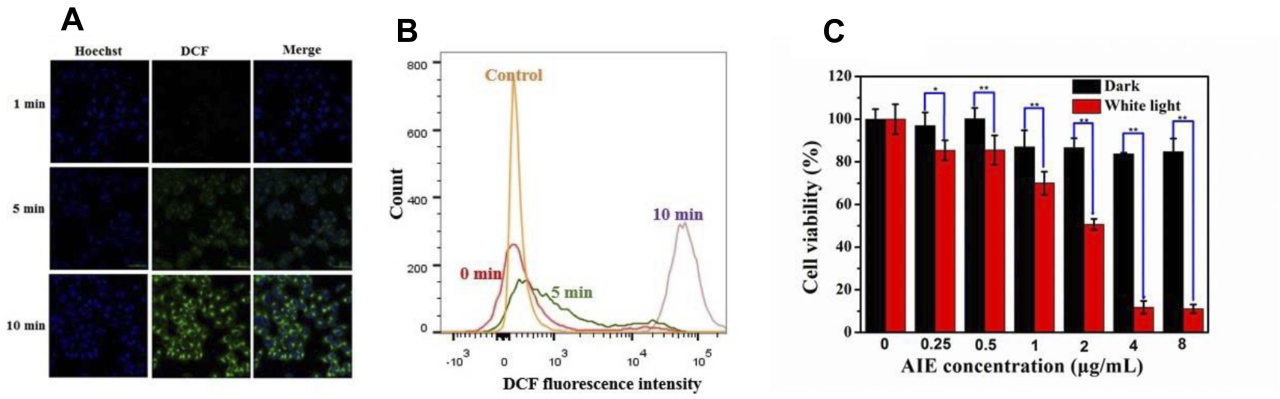

Figure 10 (**A**) Fluorescent images of HepG2 cells after incubation with SPIO/AIE@HA-*g*-PZLL nanoparticles and DCF for 12 h without or with white light irradiation. Scale bars: 200 μm. (**B**) Flow cytometry quantitative analysis of HepG2 cells treated with SPIO/AIE@HA-*g*-PZLL nanoparticles and DCF without or with white light irradiation. (**C**) Cell viability of HepG2 cells treated with different concentrations of SPIO/AIE@HA-*g*-PZLL nanoparticle without or with white light irradiation (10 min, 100 mW/cm^2) (*$p < 0.05$, **$p < 0.01$).

Abbreviations: HA-*g*-PZLL, hyaluronan/poly-(N-ε-carbobenzyloxy-L-lysine); DCF, derivative dichlorofluorescein; SPIO, superparamagnetic iron oxide; AIE, aggregation-induced emission.

with SPIO/AIE@HA-*g*-PZLL nanoparticles and DCF with white light irradiation for 0, 5 and 10 min. Cells cultured in pure culture medium were used as control group. Flow cytometry analysis showed that the green fluorescence intensity of DCF was related to the time of white light irradiation. In the absence of white light irradiation, the fluorescence intensity curve of the cells overlapped with that of the control group. When HepG2 cells received white light irradiation for 5 min, the fluorescence intensity curve shifted to the right, and a more obvious fluorescence intensity increase was observed after 10 min of white light irradiation.

Before the PDT experiment, we determined the cytotoxicity of the SPIO/AIE@HA-*g*-PZLL nanoparticles to HepG2 cells in the dark by a cell growth inhibition test. As shown in Figure 10C, HepG2 cells cocultured with different concentrations of SPIO/AIE@HA-*g*-PZLL nanoparticles up to 8 μg/mL at 37°C for 24 h in the absence of light had a survival rate of 85%. These results suggest that SPIO/AIE@HA-*g*-PZLL nanoparticles have slight cytotoxicity to cells and are suitable as theranostic nanoparticles for tumor diagnosis and treatment.

From the PDT results, we found that exposure to white light merely decreased the cell viability when the cells incubated without SPIO/AIE@HA-*g*-PZLL nanoparticles and. It should be noted that after exposure to white light, the viability of HepG2 cells was dependent on the AIE dose. When the concentration of AIE increased to 4 μg/mL, the survival rate of HepG2 cells was decreased to approximately 11%. The SPIO/

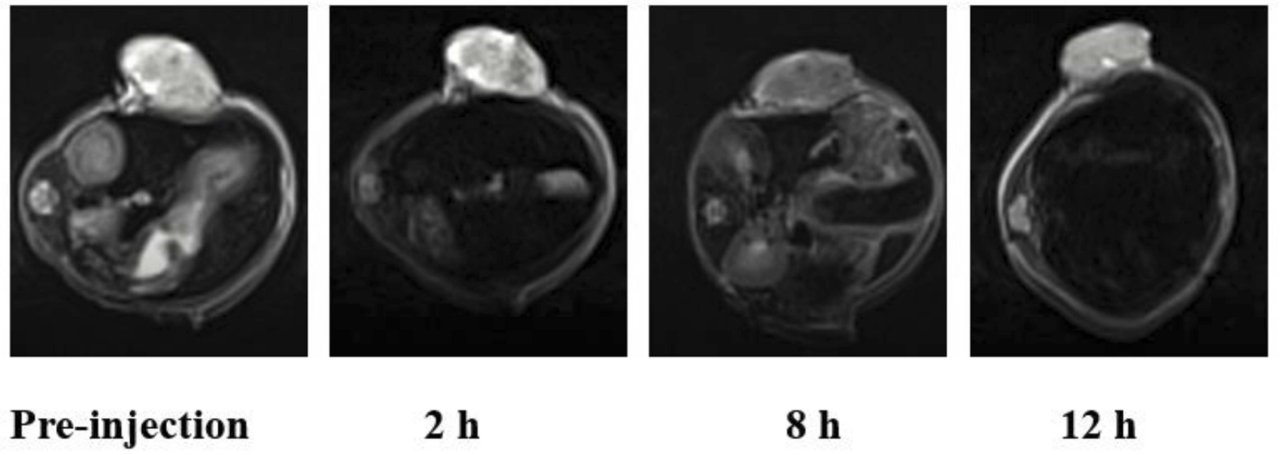

Figure 11 T_2-weighted magnetic resonance imaging of mice bearing HepG2 tumors injected with SPIO/AIE@HA-*g*-PZLL nanoparticles at a dose of 5 mg Fe per kg.
Abbreviations: HA-*g*-PZLL, hyaluronan/poly-(N-ε-carbobenzyloxy-L-lysine) derivative; SPIO, superparamagnetic iron oxide; AIE, aggregation-induced emission.

AIE@HA-*g*-PZLL nanoparticles show excellent PDT activity and great potential in tumor therapy.

In vivo MR Imaging

The SPIO/AIE@HA-*g*-PZLL nanoparticles showed good in vitro MR imaging capacity. Herein, in vivo T_2-weighted MR imaging of tumor-bearing mice was performed in a 3.0 T MR imaging scanner. As shown in Figure 11, after tail vein injection with theranostic nanoparticles at a dose of 5 mg Fe per kg, the T_2-weighted MR images of the tumor region showed obvious dark signal. Compared to the T_2-weighted MR signal in the tumor region before contrast agent injection, MR signals of the tumor region were gradually darkened likely due to the accumulation of the theranostic nanoparticles within the tumor region. At 8 h postinjection, the tumor region showed maximum contrast enhancement, indicating that the injected theranostic particles mainly accumulated in the tumor site. Afterwards the MR signals in the tumor site gradually recovered, indicating that the particles were removed from the tumor site through metabolism. These results suggested that SPIO/AIE@HA-*g*-PZLL nanoparticles have good potential as T_2-weighted MR contrasted agents for tumor diagnosis.

Conclusions

In summary, we succeeded in developing CD44-targeted MR/FL dual-modal imaging theranostic nanoparticles for image-guided PDT. These nanoparticles were obtained by the simultaneous loading of SPIO nanoparticles and AIE molecules into the core of HA-g-PZLL nanoparticles. The diameter, morphology, photophysical properties and dual-modal imaging ability of the theranostic nanoparticles were characterized in detail. These nanoparticles not only showed AIE characteristic and MR contrast enhancement ability but also efficiently generated singlet oxygen upon light irradiation. Cellular uptake experiments indicated that these theranostic nanoparticles can be efficiently taken up and are predominately present in the cytoplasm. In vitro cytotoxicity experiments showed that these nanoparticles showed that these nanoparticles had serious cytotoxicity to the growth of HepG2 cells after white light irradiation. This work provides a simple method for the preparation of theranostic nanoparticles with AIE characteristics and MR imaging contrast enhancement that can serve as a dual-modal imaging platform for image-guided tumor PDT.

Acknowledgment

This work was supported by the National Natural Science Foundation of China (81571665, 81971574), the Science Foundation of Guangzhou First People's Hospital (M2019017), the Natural Science Foundation of Guangdong Province in China (2018A030313282), Guangdong Medical Science and Research Foundation (A2019071), Guangzhou Planned Project of Science and Technology (20190401 0422, 201607010038), the Social Development Fund of Guangdong Province (2014A020212031, 2014A020212030), the Fundamental Research Funds for the Central Universities, SCUT (2018MS23) and Guangzhou General Science and Technology Project of Health and Family Planning (20191A011012, 20181A011016).

Disclosure

The authors report no conflicts of interest in this work.

References

1. Lin S-Y, Huang R-Y, Liao W-C, Chuang -C-C, Chang C-W. Multifunctional PEGylated albumin/IR780/iron oxide nanocomplexes for cancer photothermal therapy and MR Imaging. *Nanotheranostics*. 2018;2:106–116. doi:10.7150/ntno.19379
2. Dong Z, Feng L, Zhu W, et al. CaCO3 nanoparticles as an ultra-sensitive tumor-pH-responsive nanoplatform enabling real-time drug release monitoring and cancer combination therapy. *Biomaterials*. 2016;110:60–70. doi:10.1016/j.biomaterials.2016.09.025
3. Feng L, Gao M, Tao D, et al. Cisplatin-prodrug-constructed liposomes as a versatile theranostic nanoplatform for bimodal imaging guided combination cancer therapy. *Adv Funct Mater*. 2016;26:2207–2217. doi:10.1002/adfm.201504899
4. Chen Q, Chen J, Liang C, et al. Drug-induced co-assembly of albumin/catalase as smart nano-theranostics for deep intra-tumoral penetration, hypoxia relieve, and synergistic combination therapy. *J Control Release*. 2017;263:79–89. doi:10.1016/j.jconrel.2016.11.006
5. Zhu W, Dong Z, Fu T, et al. Modulation of hypoxia in solid tumor microenvironment with MnO2 nanoparticles to enhance photodynamic therapy. *Adv Funct Mater*. 2016;26:5490–5498. doi:10.1002/adfm.201600676
6. Li K, Ding D, Huo D, et al. Conjugated polymer based nanoparticles as dual-modal probes for targeted in vivo fluorescence and magnetic resonance imaging. *Adv Funct Mater*. 2012;22:3107–3115. doi:10.1002/adfm.201102234
7. Han Y, An Y, Jia G, et al. Theranostic micelles based on upconversion nanoparticles for dual-modality imaging and photodynamic therapy in hepatocellular carcinoma. *Nanoscale*. 2018;10:6511–6523. doi:10.1039/C7NR09717D
8. Lim E, Kim T, Paik S, Haam S, Huh Y, Lee K. Nanomaterials for theranostics: recent advances and future challenges. *Chem Rev*. 2015;115:327–394. doi:10.1021/cr300213b
9. Wang S, Huang P, Chen X. Stimuli-responsive programmed specific targeting in nanomedicine. *ACS Nano*. 2016;10:2991–2994. doi:10.1021/acsnano.6b00870
10. Wu X, Zhou L, Su Y, Dong C-M. Plasmonic, targeted, and dual drugs-loaded polypeptide composite nanoparticles for synergistic cocktail chemotherapy with photothermal therapy. *Biomacromolecules*. 2016;17:2489–2501. doi:10.1021/acs.biomac.6b00721
11. Tang J, Sheng Y, Hu H, Shen Y. Macromolecular MRI contrast agents: structures, properties and applications. *Prog Polym Sci*. 2013;38:462–502. doi:10.1016/j.progpolymsci.2012.07.001

12. Thurecht KJ. Polymers as probes for multimodal Imaging with MRI. *Macromol Chem Phys*. 2012;213:2567–2572. doi:10.1002/macp.201200420
13. Yu MK, Park J, Jon S. Targeting strategies for multifunctional nanoparticles in cancer imaging and therapy. *Theranostics*. 2012;2:3–44. doi:10.7150/thno.3463
14. Huang J, Zhang H, Yu Y, et al. Biodegradable self-assembled nanoparticles of poly (d,l-lactide-co-glycolide)/hyaluronic acid block copolymers for target delivery of docetaxel to breast cancer. *Biomaterials*. 2014;35:550–566. doi:10.1016/j.biomaterials.2013.09.089
15. Yin S, Huai J, Chen X, et al. Intracellular delivery and antitumor effects of a redox-responsive polymeric paclitaxel conjugate based on hyaluronic acid. *Acta Biomater*. 2015;26:274–285. doi:10.1016/j.actbio.2015.08.029
16. Thomas RG, Moon MJ, Lee H, et al. Hyaluronic acid conjugated superparamagnetic iron oxide nanoparticle for cancer diagnosis and hyperthermia therapy. *Carbohydr Polym*. 2015;131:439–446. doi:10.1016/j.carbpol.2015.06.010
17. Upadhyay KK, Meins JFL, Misra A, et al. Biomimetic doxorubicin loaded polymersomes from hyaluronan-block-Poly(γ-benzyl glutamate) copolymers. *Biomacromolecules*. 2009;10:2802–2808. doi:10.1021/bm9006419
18. Šmejkalová D, Nešporová K, Huerta-Angeles G, et al. Selective in vitro anticancer effect of superparamagnetic iron oxide nanoparticles loaded in hyaluronan polymeric micelles. *Biomacromolecules*. 2014;15:4012–4020. doi:10.1021/bm501065q
19. Yang R-M, Fu C-P, Fang J-Z, et al. Hyaluronan-modified superparamagnetic iron oxide nanoparticles for bimodal breast cancer imaging and photothermal therapy. *Int J Nanomedicine*. 2017;12:197–206. doi:10.2147/IJN.S121249
20. Yang H, Wang N, Mo L, et al. Reduction sensitive hyaluronan-SS-poly(ε-caprolactone) block copolymers as theranostic nanocarriers for tumor diagnosis and treatment. *Mater Sci Eng C*. 2019;98:9–18. doi:10.1016/j.msec.2018.12.132
21. Bhirde A, Xie J, Swierczewska M, Chen X. Nanoparticles for cell labeling. *Nanoscale*. 2011;3:142–153. doi:10.1039/C0NR00493F
22. Hu D, Chen L, Qu Y, et al. Oxygen-generating hybrid polymeric nanoparticles with encapsulated doxorubicin and chlorin e6 for trimodal imaging-guided combined chemo-photodynamic therapy. *Theranostics*. 2018;8:1558–1574. doi:10.7150/thno.22989
23. Qi H, Li Z, Du K, et al. Transferrin-targeted magnetic/fluorescence micelles as a specific bi-functional nanoprobe for imaging liver tumor. *Nanoscale Res Lett*. 2014;9:595. doi:10.1186/1556-276X-9-595
24. Wang L, Zhang P, Shi J, et al. Radiofrequency-triggered tumor-targeting delivery system for theranostics application. *ACS Appl Mater Interfaces*. 2015;7:5736–5747. doi:10.1021/am507898z
25. Zeng Y, Zhang D, Wu M, et al. Lipid-AuNPs@PDA nanohybrid for MRI/CT imaging and photothermal therapy of hepatocellular carcinoma. *ACS Appl Mater Interfaces*. 2014;6:14266–14277. doi:10.1021/am503583s
26. Hao N, Sun C, Wu Z, et al. Fabrication of polymeric micelles with aggregation-induced emission and forster resonance energy transfer for anticancer drug delivery. *Bioconjug Chem*. 2017;28:1944–1954. doi:10.1021/acs.bioconjchem.7b00274
27. Huang M, Yu R, Xu K, et al. An arch-bridge-type fluorophore for bridging the gap between aggregation-caused quenching (ACQ) and aggregation-induced emission (AIE). *Chem Sci*. 2016;7:4485–4491. doi:10.1039/C6SC01254J
28. Yuan WZ, Lu P, Chen S, et al. Changing the behavior of chromophores from aggregation-caused quenching to aggregation-induced emission: development of highly efficient light emitters in the solid state. *Adv Mater*. 2010;22:2159–2163. doi:10.1002/adma.200904056
29. Mei J, Leung NLC, Kwok RTK, Lam JWY, Tang BZ. Aggregation-induced emission: together we shine, united we soar! *Chem Rev*. 2015;115:11718–11940. doi:10.1021/acs.chemrev.5b00263
30. Qian J, Tang BZ. AIE luminogens for bioimaging and theranostics: from organelles to animals. *Chem*. 2017;3:56–91. doi:10.1016/j.chempr.2017.05.010
31. Li K, Ding D, Prashant C, et al. Gadolinium-functionalized aggregation-induced emission dots as dual-modality probes for cancer metastasis study. *Adv Healthc Mater*. 2013;2:1600–1605. doi:10.1002/adhm.201300135
32. Chen Y, Li M, Hong Y, Lam JWY, Zheng Q, Tang BZ. Dual-Modal MRI contrast agent with aggregation-induced emission characteristic for liver specific imaging with long circulation lifetime. *ACS Appl Mater Interfaces*. 2014;6:10783–10791. doi:10.1021/am502282f
33. Tian S, Liu G, Wang X, Zhang G, Hu J. pH-responsive tumor-targetable theranostic nanovectors based on core crosslinked (CCL) micelles with fluorescence and magnetic resonance (MR) dual imaging modalities and drug delivery performance. *Polymers*. 2016;8:226. doi:10.3390/polym8060226
34. Yan L, Zhang Y, Ji G, et al. Multifunctional polymer nanoparticles: ultra bright near-infrared fluorescence and strong magnetization and their biological applications. *RSC Adv*. 2016;6:65426–65433. doi:10.1039/C6RA07520G
35. Yuan Y, Zhang C, Kwok RTK, et al. Photodynamic therapy: light-up probe for targeted and activatable photodynamic therapy with real-time in situ reporting of sensitizer activation and therapeutic responses (Adv. Funct. Mater. 42/2015). *Adv Funct Mater*. 2015;25:6691. doi:10.1002/adfm.201570273
36. Yuan Y, Zhang C-J, Kwok RTK, et al. Light-up probe for targeted and activatable photodynamic therapy with real-time in situ reporting of sensitizer activation and therapeutic responses. *Adv Funct Mater*. 2015;25:6586–6595. doi:10.1002/adfm.201502728
37. Agostinis P, Berg K, Cengel KA, et al. Photodynamic therapy of cancer: an update. *CA Cancer J Clin*. 2011;61:250–281. doi:10.3322/caac.20114
38. Li M, Gao Y, Yuan Y, et al. One-step formulation of targeted aggregation-induced emission dots for image-guided photodynamic therapy of cholangiocarcinoma. *ACS Nano*. 2017;11:3922–3932. doi:10.1021/acsnano.7b00312
39. Gao M, Tang BZ. Aggregation-induced emission probes for cancer theranostics. *Drug Discov Today*. 2017;22:1288–1294. doi:10.1016/j.drudis.2017.07.004
40. Schatz C, Louguet S, Meins JL, Lecommandoux S. Polysaccharide-block-polypeptide copolymer vesicles: towards synthetic viral capsids. *Angew Chem*. 2009;48:2572–2575. doi:10.1002/anie.200805895
41. Agut W, Agnaou R, Lecommandoux S, Taton D. Synthesis of block copolypeptides by click chemistry. *Macromol Rapid Commun*. 2008;29:1147–1155. doi:10.1002/marc.200800123
42. Dicker KT, Gurski LA, Pradhanbhatt S, Witt RL, Farachcarson MC, Jia X. Hyaluronan: a simple polysaccharide with diverse biological functions. *Acta Biomater*. 2014;10:1558–1570. doi:10.1016/j.actbio.2013.12.019
43. Chang L, Deng L, Wang W, et al. Poly(ethyleneglycol)-b-Poly(ε-caprolactone-co-γ-hydroxyl-ε- caprolactone) bearing pendant hydroxyl groups as nanocarriers for doxorubicin delivery. *Biomacromolecules*. 2012;13:3301–3310. doi:10.1021/bm301086c
44. Yang X, Chen Y, Yuan R, et al. Folate-encoded and Fe3O4-loaded polymeric micelles for dual targeting of cancer cells. *Polymer*. 2008;49:3477–3485. doi:10.1016/j.polymer.2008.06.005
45. Zheng Y, Lu H, Jiang Z, et al. Low-power white light triggered AIE polymer nanoparticles with high ROS quantum yield for mitochondria-targeted and image-guided photodynamic therapy. *J Mater Chem B*. 2017;5:6277–6281. doi:10.1039/C7TB01443K

46. Bourre L, Thibaut S, Briffaud A, et al. Indirect detection of photosensitizer ex vivo. *J Photochem Photobiol B*. 2002;67:23–31. doi:10.1016/S1011-1344(02)00279-8
47. Yang X, Grailer JJ, Rowland IJ, et al. Multifunctional SPIO/DOX-loaded wormlike polymer vesicles for cancer therapy and MR imaging. *Biomaterials*. 2010;31:9065–9073. doi:10.1016/j.biomaterials.2010.08.039
48. Shirasu N, Nam SO, Kuroki M. Tumor-targeted photodynamic therapy. *Anticancer Res*. 2013;33:2823–2831.
49. Upadhyay KK, Bhatt AN, Mishra AK, et al. The intracellular drug delivery and anti tumor activity of doxorubicin loaded poly(γ-benzyl L-glutamate)-b-hyaluronan polymersomes. *Biomaterials*. 2010;31:2882–2892. doi:10.1016/j.biomaterials.2009.12.043